https://doi.org/10.5194/essd-2025-678
Preprint. Discussion started: 4 January 2026

Open Access Earth System Science Data Discussions

Bedrock topography and ice thickness distribution of three major Patagonian outlet glaciers unveiled by helicopter-borne ground penetrating radar

Moritz Koch[1], Jorge Berkhoff[1], Norbert Blindow[1], David Farías-Barahona[2], Pedro Skvarca[3], Johannes J. Fürst[1], Matthias Braun[1]

[1]Department of Geography, Friedrich-Alexander-Universität Erlangen-Nürnberg, Erlangen, 91058, Germany
[2]Department of Geography, University of Concepcíon, Concepcíon, 4030000, Chile
[3]Glaciarium – Glacier Interpretive Center, El Calafate, 9201, Argentina

Correspondence to: Moritz Koch (Moritz.Koch@fau.de)

Abstract.

We present the first helicopter-borne ground-penetrating radar dataset over Glaciar Viedma, Upsala, and Perito Moreno, three of the largest outlet glaciers of the Southern Patagonian Icefield in South America. The dataset comprises 116.021 individual ice-thickness measurements along 232 km of flight tracks. Data were acquired during two campaigns in March and April 2022 as well as in October 2024 using a 25 MHz shielded broadband antenna deployed as a helicopter sling load. For the first time, we reveal the complex subglacial topography of these glaciers in their lower regions and measured bed reflections at Glaciar Upsala in depths of up to 800 m. The newly obtained measurements were incorporated into an ice-thickness reconstruction method to derive glacier-wide ice-thickness distribution maps and the corresponding bedrock topography. The latter exerts primary control on the response of water-terminating glaciers to a changing climate. Our 100-m gridded ice-thickness maps indicate that the three glaciers had a combined ice volume of 831.14 km³ in the year 2000. The dataset and the well-constrained glacier-wide grids provide a valuable basis for future studies aiming to better understand the mechanisms driving glacier retreat and the susceptibility of these large outlet glaciers to climate change. All data are publicly available at Zenodo (10.5281/zenodo.17802904; (Koch et al., 2025a)).

https://doi.org/10.5194/essd-2025-678
Preprint. Discussion started: 4 January 2026

1 Introduction

The recession and mass loss of mountain glaciers and ice caps are clear indicators of anthropogenic climate change (Bojinski et al., 2014). The reduction of glaciated areas affects ecosystems, freshwater availability both locally and downstream, and regional water cycles, and represents a key contributor to global sea-level rise (Bamber et al., 2018; Dorigo et al., 2021; Bosson et al., 2023; Rounce et al., 2023). Projections suggest that global glacier volume may decrease by 28 - 49% by the end of the 21st century under the SSP2-6.0 and SSP8-5.0 scenarios, respectively (Zekollari et al., 2024). However, current glacier mass loss varies substantially on regional scales (The GlaMBIE Team et al., 2025).

The Patagonian Icefields in South America, consisting of the Northern (NPI) and Southern Patagonian Icefield (SPI), exhibit some of the highest glacier mass loss rates worldwide (Braun et al., 2019; Hugonnet et al., 2021; The GlaMBIE Team et al., 2025). By 2100, glaciers in the Patagonian Andes are projected to lose 46 – 67% of their volume, which may be underestimated since current models omit key processes like frontal ablation (Aguayo et al., 2024). The largest contributions to this mass loss originate from outlet glaciers that terminate either in the Pacific fjords on the western side or in proglacial lakes on the eastern side of the icefields (Minowa et al., 2021a). Despite their proximity, individual outlet glaciers display contrasting retreat behaviour and strong intra-icefield variability in mass change (Abdel Jaber et al., 2019; McDonnell et al., 2022). Among several contributing factors, the subglacial topography of the glacier basins plays a key role in explaining this heterogeneity (Benn et al., 2007; Frank et al., 2022). Bathymetric surveys of recently retreated outlets have shown that ice-dynamic losses are the dominant control on glacier retreat, largely governed by lake depth and bed shape (Minowa et al., 2023b).

Accurate knowledge of glacier ice thickness and bedrock topography is therefore essential to predict future glacier evolution and to disentangle the relative influence of climatic forcing and ice dynamics, particularly for water-terminating glaciers. Results from ice-thickness model intercomparison studies demonstrate that inversion outcomes diverge widely in the absence of in-situ constraints, underlining the importance of direct bedrock measurements for calibrating and validating ice-thickness reconstruction approaches (Farinotti et al., 2017, 2021).

https://doi.org/10.5194/essd-2025-678
Preprint. Discussion started: 4 January 2026

Although gravimetric surveys cover some areas of the icefield plateau, the bedrock topography of the lower outlet zones remains largely unknown for many glacier basins, particularly in the central and southern regions (Fürst et al., 2024a; Gourlet et al., 2016). This knowledge gap arises from the general inaccessibility of glacier tongues and their heavily crevassed surfaces. Combined with the steep mountainous terrain surrounding the outlets, these conditions make helicopter-borne ground-penetrating radar (GPR) surveys the only practical means to obtain extensive, high-density ice-thickness measurements over large areas.

This paper presents helicopter-borne ground-penetrating radar (GPR) measurements collected over three of the largest western outlet glaciers of the Southern Patagonian Icefield (SPI), which have exhibited markedly different retreat patterns over the past decades. During two survey campaigns in 2022 and 2024, we acquired GPR data over Glaciar Perito Moreno, Viedma, and Upsala using a 25 MHz antenna suspended beneath a helicopter, completing a total of six survey flights. In total, we collected 116.021 measurement points, corresponding to approximately 232 km of ice-thickness profiles. We provide a detailed description of the pre-processing and processing steps applied to the GPR data, together with a comprehensive uncertainty analysis. Furthermore, we integrate the acquired measurements into an existing ice-thickness reconstruction framework to derive continuous ice-thickness distributions and reveal the bedrock topography of the three glacier basins.

The resulting datasets form a foundation for future modelling efforts aimed at disentangling the primary drivers of the exceptional and heterogeneous mass loss observed in the region and at improving the understanding of ice dynamics in lacustrine glacier systems within one of the wettest regions on Earth.

2 Study site

The SPI is located in the south of South America expanding roughly 360 km from 48° S to 51.5° S and between 74° W to 73° W (see Fig. 1a&b) (Casassa et al., 2014). It is the largest icefield in the Southern Hemisphere outside of Antarctica (Glasser et al., 2011). The SPI lies in the mid-latitudes and experiences a strongly maritime, westerly-dominated climate with extreme west–east gradients (Sauter, 2020). It is characterized by subpolar oceanic on the windward side, alpine polar over the icefield and cool, semi-

https://doi.org/10.5194/essd-2025-678
Preprint. Discussion started: 4 January 2026

Open Access Earth System Science Data Discussions

arid conditions in the lee (Beck et al., 2018; Garreaud et al., 2013). The westerlies transport vast amounts of moist maritime air from the Pacific Ocean toward the Andean mountain range (Garreaud et al., 2013; Sauter, 2020). When the air masses encounter the steep Andean topography, they produce a strong orographic precipitation on the western (windward) slopes, resulting in annual precipitation rates of roughly 5 – 6 m w.e. yr^{-1}, with local maxima reaching up to 10 m w.e. yr^{-1} (Sauter, 2020). On the eastern side of the ice divide, rain shadow and föhn effects sharply reduce precipitation to a few hundred

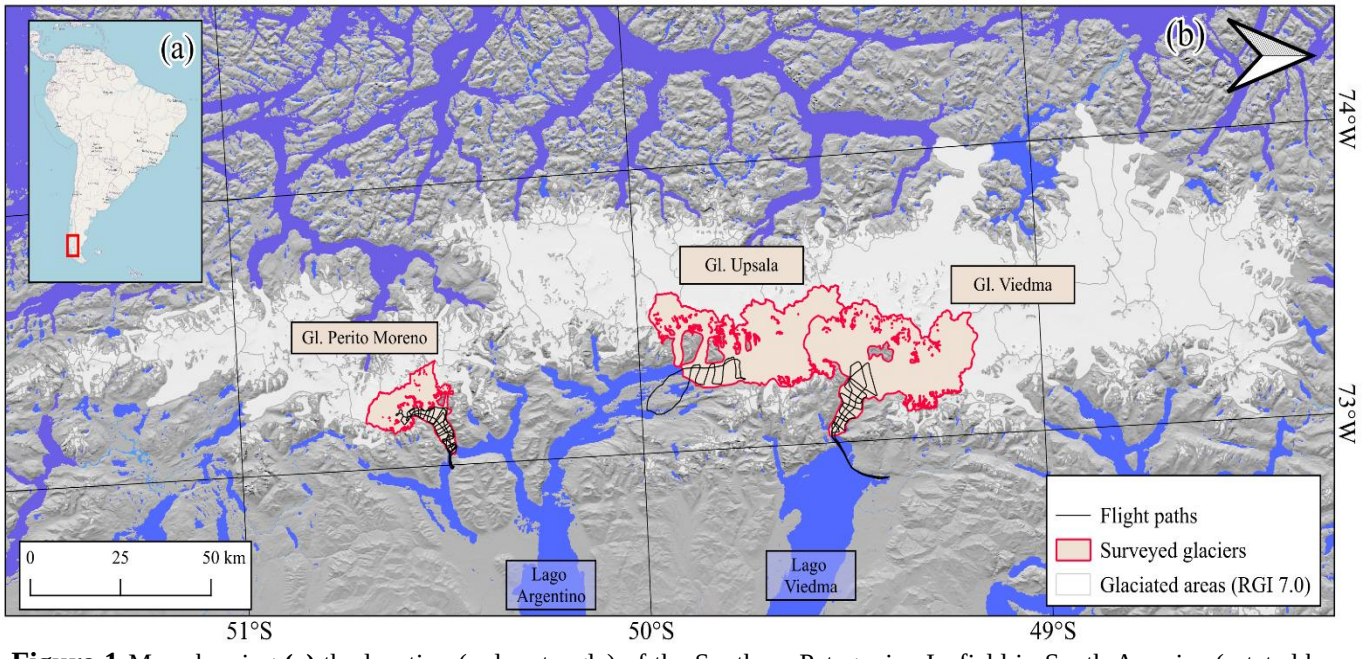

Figure 1 Map showing **(a)** the location (red rectangle) of the Southern Patagonian Icefield in South America (rotated by 90°). **(b)** Shows the Southern Patagonian Icefield and the location of the surveyed Glaciar Perito Moreno, Upsala and Viedma. The black lines indicate the GPS flight tracks of the helicopter-borne surveys. The glaciated areas and boundaries are indicated according to the RGI 7.0 (RGI Consortium, 2023), but outlines of large water terminating glaciers were manually updated to the year 2024 based on optical imagery. The background consists of a hill shaded SRTM DEM (Farr et al., 2007) and the SRTM water body mask (Carroll et al., 2009). The map in **(a)** is map data from ©OpenStreetMap Distributed under the Open Data Commons Open Database License (ODbL) v1.0.

millimetres per year (Viale and Garreaud, 2015). Here, in the period from 1996 to 2020 the decadal warming trend in proximity of Glaciar Perito Moreno's terminus was +0.28 ± 0.18 °C, with the strongest trend during austral summer with warming rates of +0.318 ± 0.18 °C per decade (Minowa et al., 2023a).

https://doi.org/10.5194/essd-2025-678
Preprint. Discussion started: 4 January 2026


Open Access Earth System Science Data Discussions

The SPI is characterized by large outlet glaciers that are flowing into fjords in the west or lakes in the east (Aniya et al., 1997). Generally, glaciers in the region have a large mass balance gradient due to their strong accumulation and surface ablation (Lenaerts et al., 2014; Schaefer et al., 2015). Glaciers terminating in water lose mass by calving at their terminus and melt below the water level (Minowa et al., 2021b). Three of the largest outlet glaciers on the eastern side are Glaciar Viedma, Upsala, and Perito Moreno (see Fig. 1b). Glaciar Viedma terminates in Lago Viedma at 252 m a.s.l. (lake level), while Glaciar Upsala and Perito Moreno terminate in Lago Argentino at 178 m a.s.l. (lake level). The accumulation zones of Glaciar Viedma and Upsala reach above 3200 m a.s.l. (according to the Copernicus DEM) and cover approximately 896 km² and 779 km², respectively, as in 2024. The accumulation zone of Glaciar Perito Moreno extends up to 2800 m a.s.l. and covered an area of 256 km² in 2024 (European Space Agency and Airbus, 2022; RGI Consortium, 2023). While being subject to the same, or at least similar, climatic forcing due to their close proximity, the retreat patterns over the past decades have differed substantially. Viedma Glacier had a gradual increase in retreat rates from 2000 to 2012 averaging at 33 m a^{-1} and displaying a subsequent acceleration from 2012 to 2021 to 200 m a^{-1} (Minowa et al., 2023c). Upsala Glacier on the other hand retreated in the 1990 s by up to 700 m a^{-1} and an additional 2.9 km between 2008 and 2011 (Naruse et al., 1997; Sakakibara et al., 2013). From 2011 onwards, retreat rates have slowed down to less than 100 m a^{-1} until 2022 (Minowa et al., 2023c). Glaciar Perito Moreno, on the other hand, did not retreat or thin until 2019; in fact, it advanced by several tens of meters onto a peninsula at its central terminus, damming the Brazo Rico, a lake arm of Lago Argentino (Skvarca and Naruse, 2006; Stuefer et al., 2007; Koch et al., 2025b). Since 2019, however, it started to retreat at its northern and south-eastern margin by up to 800 meters, accompanied by increased thinning rates and ice velocity (Koch et al., 2025b). Besides bathymetric measurements conducted after glacier front recession, the bed topography of these three glaciers is largely unknown (Minowa et al., 2023c). At Glaciar Perito Moreno a seismic measurement was conducted in 1996 and a single borehole was drilled ~5 km from today's terminus (Stuefer et al., 2007; Sugiyama et al., 2011). Most regions of the ice field's plateau were surveyed in 2012 and 2016 with airborne gravity surveys, however the glacial trunks of Glaciar Perito Moreno, Upsala and Viedma remained uncovered (Millan et al., 2019).

https://doi.org/10.5194/essd-2025-678
Preprint. Discussion started: 4 January 2026

3 Methods and data

3.1 Ice thickness measurements

The data presented in this paper were acquired during two field campaigns in 2022 and 2024. In total, we conducted six survey flights: three over Glaciar Perito Moreno, two over Glaciar Viedma, and one over Glaciar Upsala. The latter was surveyed on 20 October 2024. Measurements on Glaciar Perito Moreno were acquired on 19 and 21 March 2022, and Glaciar Viedma was surveyed on 4 April 2022. Altogether, we acquired 393 km of glacier-profile data: 149 km on Glaciar Viedma, 73 km on Glaciar Upsala, and 171 km on Glaciar Perito Moreno. Because Patagonian outlet glaciers are temperate and thus contain substantial amounts of liquid water, such as water pockets or intraglacial channels that cause strong backscattering of electromagnetic waves, we employed a low-frequency radar system (Blindow et al., 2011). In addition to the temperate ice conditions, the main glacier trunks are highly crevassed, making airborne systems the only feasible means for large-scale data acquisition. Consequently, we deployed a shielded bistatic antenna with a center frequency of 25 MHz, suspended beneath a helicopter as a sling load (Fig. 2). The antenna structure measures 6 × 4 × 1 m and weighs about 300 kg. Although comparatively heavy, a shielded system reduces transmitter-receiver coupling and improves signal and imaging quality (Gao et al., 2019). Furthermore, the directed emission of shielded antennas enhances the coupling of energy into the ground, allowing for greater depth penetration (Blindow et al., 2011). The sling load is designed for operation at a true airspeed of approximately 70 km h^{-1}. At this speed, the two rear suspension ropes, being longer than those at the front, tilt the antenna into a horizontal orientation

Figure 2 Picture shows the 25 MHz antenna of the FAU attached to a Eurocopter AS355 Écureuil 2

https://doi.org/10.5194/essd-2025-678
Preprint. Discussion started: 4 January 2026

due to aerodynamic drag. Two horizontal flaps at the rear of the frame (Fig. 2) align the antenna in the flight direction. The surveys were conducted at a target flight altitude of 30 - 40 m above the glacier surface. The antenna was equipped with a laser altimeter, and the measured height above ground was displayed in real time on a cockpit monitor. Although slightly modified for the Friedrich-Alexander-University, this system design has proven its viability in several prior studies and performs reliably in deep, temperate ice (Blindow et al., 2010, 2012; Lippl et al., 2019; Rutishauser et al., 2016). At the receiver, radar backscatter is digitized immediately (A/D sampling at 400 MHz; 4096 samples per trace). Each trace is formed by coherent stacking of 256 pulses. The data stream is sent to the cabin via a fiber-optic link for real-time monitoring and recording. With a sampling rate of 10 Hz and an average airspeed of approximately 70 km h^{-1}, the along-track spacing is then approximately 2 m per trace, i.e., roughly 500 traces per kilometer. For accurate georeferencing, a GNSS rover is mounted at the center of the antenna and, in post-processing, its time series is synchronized with the GPR system's internal clock.

3.2 Data processing and interpretation

To provide a precise georeferencing for the GPR measurements, we used two Leica GS16 multi-frequency GNSS receivers. A GNSS base station was deployed near each of the three study glaciers, and a rover antenna was mounted at the center of the radar frame. All GNSS data were post-processed in Trimble Business Center (TBC). Base-station coordinates were determined via precise point positioning (PPP) with an accuracy of ±0.05 m, and the rover trajectory were computed with kinematic post-processing to ±0.10 m, ensuring that all GPR measurements are tied to the WGS84 global coordinate system.

Before processing, the GPR data were time-synchronized with the GNSS. We first corrected the constant GPST–UTC offset of 18 s (applicable to both campaigns) and then aligned GNSS time with the GPR internal clock. Because GNSS was logged at 1 Hz, radar files were trimmed to start and end on full-second boundaries prior to matching. To verify timing, we compared the lift-off time from the rover GNSS with the laser altimeter mounted at the rear of the antenna; once consistent, the datasets were processed in REFLEXW v8.1 (Sandmeier geophysical research).

The rest of the processing chain was entirely done in REFLEXW and identical processing steps and parameterisation was applied to all flights. The processing chain consists of:

https://doi.org/10.5194/essd-2025-678
Preprint. Discussion started: 4 January 2026

1. **Repositioning**: the data points (of each flight) were repositioned into equidistant traces.
2. **Sub setting**: the data was divided into partially overlapping strips (one transect) to reduce processing time.
3. **Time correction**: a time shift was applied to all traces individually to account for the radar's zero time.
4. **Background noise removal**: Coherent noise was removed by calculating a spatial average of 201 traces and subtracting it from each trace.
5. **Bandpass filtering**: High-frequency radio noise and spikes were filtered using a bandpass filter with a 10 MHz low cut-off and 40 MHz high cut-off.
6. **Amplitude compensation**: A gain function was applied to correct for geometric spreading and absorption losses, and small amplitudes were further enhanced using an average energy decay function derived from the mean amplitude decay curve of all traces.
7. **Manual layer determination**: Air and ice layers were manually delineated by tracing surface reflections. With the air and ice layer a 2D velocity model was created with wave propagation of 0.3 m ns^{-1} in air and 0.168 m ns^{-1} in ice.
8. **2D migration**: Using the 2D velocity model, a 2D migration by diffraction stacking was performed to focus scattered amplitudes and improve interpretability.
9. **Air-Layer correction**: Each trace was statistically corrected based on the air-layer distances, shifting traces upward (negative y-direction).
10. **Interpretation of the bedrock reflection**: Two-way travel times in ice were interpreted (by a single annotator) and converted into ice thickness values along each profile.
11. **Merging**: The results from all data blocks were merged into a single vector containing the final processed dataset.

https://doi.org/10.5194/essd-2025-678
Preprint. Discussion started: 4 January 2026

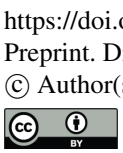

Figures 3 and 4 show the results of the processing chain for two cross sections over Glaciar Upsala (Fig. 3c) and Glaciar Viedma (Fig. 4c). In Figure 3a, distinct radar backscatter from the bedrock is visible. On the left side of the radargram, however, the bedrock is not clearly resolved due to the large amount of debris in this section (see Fig. 3c). The cross section reveals a steep and deep glacial trough with ice

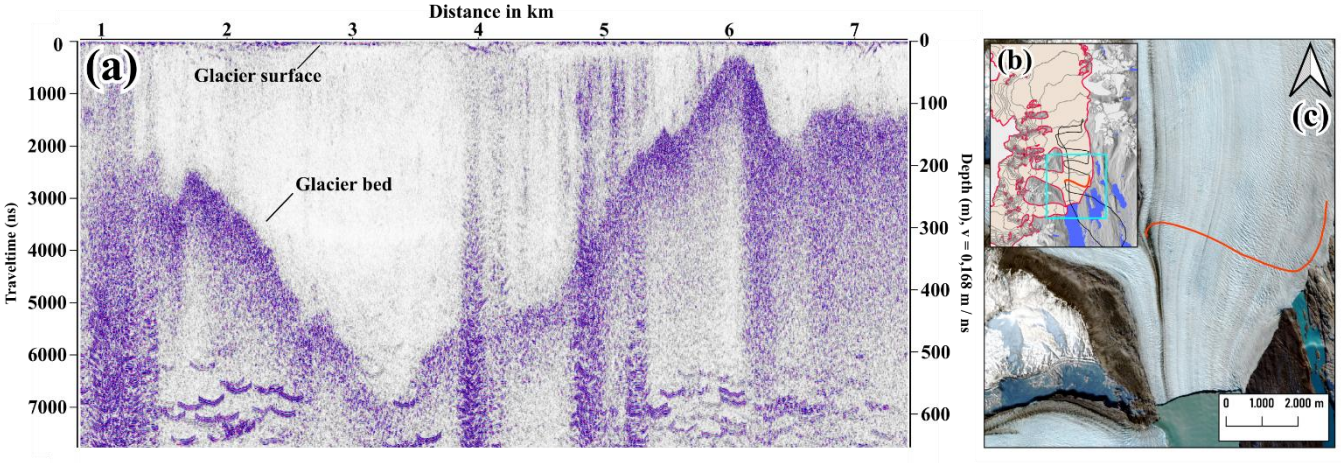

Figure 3 Radargram **(a)** acquired along a cross-section located approximately 2 km upstream from the terminus of Glaciar Upsala. The corresponding flight line is shown in panel **(c)**, with its location indicated in panel **(b)**. In the left portion of the radargram, the influence of the thick debris cover is evident, as bedrock reflections become indistinct or no longer discernible. Background imagery in **(c)** is a Sentinel-2 scene acquired on 28.08.2025.

thicknesses close to 600 m in the central part. Between kilometer 4 and 5 of the transect, the radar signal is attenuated by the surface morphology of the glacier. Figure 4a shows a transect over Glaciar Viedma.

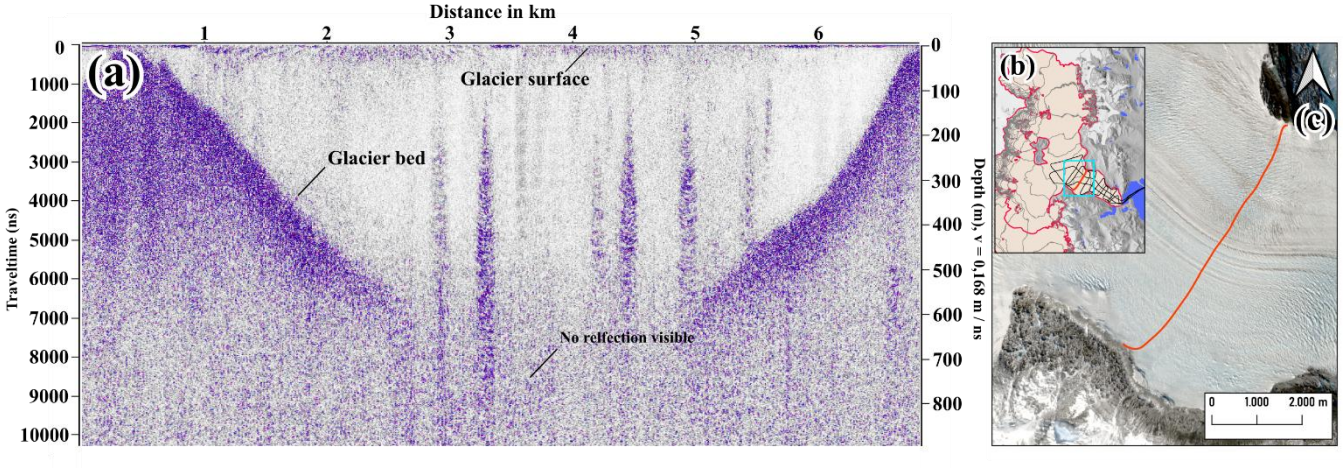

Figure 4 Radargram **(a)** from a cross section of Glaciar Viedma **(c)**. Location of the cross section is indicated in **(b)**. In the central part of the cross section no bedrock reflections are identifiable. Background imagery in **(c)** is a Sentinel-2 scene acquired on 03.09.2025.

https://doi.org/10.5194/essd-2025-678
Preprint. Discussion started: 4 January 2026

Here, clear bedrock reflections are visible towards both glacier margins, but no distinct reflections are observed in the central part of the transect. This pattern is consistent across all transects of Glaciar Viedma. The backscatter fades out at approximately 600–650 m of ice thickness, which is lower than the maximum thickness measured at Glaciar Perito Moreno and Glaciar Upsala (both exceeding 700 m).

3.3 Ice thickness measurement uncertainty

To quantify the uncertainty in the ice-thickness measurements, we applied an established error propagation approach following Lapazaran et al., 2016. In their framework, the total uncertainty of each data point is divided into two components

$$\varepsilon_{H,data_i} = \sqrt{\varepsilon_{H\ GPR_i}^2} + \varepsilon_{H\ xy_i}^2$$

The error of the value from the radar measurement (ε_{HGPR}) and the error in thickness due to horizontal positioning errors ($\varepsilon_{H,xy}$) .

The positioning error $\varepsilon_{H,xy}$ primarily depends on the acquisition velocity and the local bed slope, which explains the higher uncertainties observed over steeper bed topography. We estimated the local bed slope as:

$$\varepsilon_{H,xy} = \left|\frac{dH}{dx}\right| \times \varepsilon_{xy}$$

Some sections do not have continuous picks (e.g. Fig. 4a), which could result in unrealistic calculations of the slope. These (single) points were discarded after the error calculations. The radar error $\varepsilon_{H,GPR}$ was calculated as:

$$\varepsilon_{H,GPR} = \frac{1}{2}\sqrt{c^2 \times \varepsilon_t^2 + t^2 \times \varepsilon_c^2}$$

where c the radar-wave velocity in temperate ice 0.168 m ns^{-1}, t is the two-way travel time (TWTT), ε_t the picking uncertainty (in seconds) and ε_c the velocity uncertainty. As our acquisitions were conducted almost entirely over snow-free ice, we did not account for varying propagation velocities within firn or snow layers. Although the profiles over Glaciar Perito Moreno reached into the accumulation area,

https://doi.org/10.5194/essd-2025-678
Preprint. Discussion started: 4 January 2026

reflections in these upper sections were not interpretable and were therefore excluded from the bedrock delineation (see section 4.3.1).

3.4 Data description

The ice thickness data points (see Table 1) were organized in a comma-separated (.csv) file following the Glacier Thickness Database format (World Glacier Monitoring Service - WGMS), 2020). The file is available in a public repository (with an assigned DOI), together with the ice thickness reconstructions and bedrock maps. Most attribute field names are self-explanatory and follow the structure described in Table 1.

Table 1: Data description of the measurement data and the respective unit format.

ATTRIBUTE FIELD	UNIT / FORMAT	DESCRIPTION
EASTING	m	UTM zone 18s coordinate point east
NORTHING	m	UTM zone 18s coordinate point north
GLACIER	Text string	Name of the surveyed glacier
ACQUI_DATE	YYYY-MM-DD	Acquisition date
SURFACE_EL	m a.s.l.	Surface elevation measured at acquisition date
TRAVELTIME	ns	Two-way signal travel-time in nano seconds
ICETHICKN	m	Ice thickness value at acquisition date
BEDROCK_EL	m a.s.l.	Bedrock elevation in m a.s.l.
UNCERTAINTY	m	Ice thickness uncertainty
GLIMSID	Text string	Glims identifier
RGIID7	Text string	RGI v.7 identifier

The geographic reference system is provided in easting and northing coordinates for UTM Zone 18S. The acquisition date is listed for each survey, and the surface elevation corresponds to the measured surface elevation on that specific day. The uncertainty represents the total uncertainty as described in Section 3.3. The travel time refers to the two-way travel time of the radar wave within the ice with the air layer removed prior to calculation.

https://doi.org/10.5194/essd-2025-678
Preprint. Discussion started: 4 January 2026

Additionally, we provide the entire dataset in an unprocessed state. The data are stored in folders containing all flights for the three glaciers. The only processing step applied was merging the updated coordinate points with the traces by importing them into REFLEXW v8.1. The traces were then made equidistant and stored in individual folders for each surveyed glacier.

3.5 Ice thickness reconstruction

In addition to our measurements, we incorporated them into an established ice-thickness reconstruction method that has been applied in several regions and is able to incorporate observational constraints (Farinotti et al., 2021; Fürst et al., 2017, 2018, 2024b; Sommer et al., 2023). By doing so, we can generate a thickness map for entire glacial basins (for the year 2000), as well as maps of the bedrock topography. The two-step method is primarily based on the principle of mass conservation (Fürst et al., 2017). In the first step, we employ two complementary approaches to infer glacier-wide ice thickness fields without using surface velocity data (Fürst et al., 2017, 2018). The first is an iterative flux-based method, which formulates the problem in terms of ice flux and converts it to thickness using the Shallow Ice Approximation (SIA). The conversion depends on a spatially variable viscosity parameter estimated at locations with ice thickness measurements. A viscosity re-scaling is applied to improve estimates in areas distant from observations (Sommer et al., 2023). The thickness fields from the SIA serve as boundary conditions for the second step, where they are refined in regions with surface velocities exceeding 100 m yr^{-1}. Comparing the modelled ice thickness field values to the observed values (Appendix Fig. 2) the reconstructed ice thickness fields have a misfit of 10.7 m (σ = 77.4 m, n = 116.021). The triangular model mesh has a 400 m resolution, refined to 200 m near observations, and the final results are interpolated to a 100 m rectangular grid.

3.6. Ice thickness reconstruction uncertainty

In order to assess the uncertainties in the ice-thickness reconstruction method described above, we performed a set of model runs with varying parameterisations of the input fields. The main error sources propagating through the reconstruction are the uncertainties in the measurements (as described in Section 3.3.) and the uncertainties introduced by extrapolating ice viscosity in areas without observations. In

https://doi.org/10.5194/essd-2025-678
Preprint. Discussion started: 4 January 2026

addition, we perturbed the surface mass-balance gradient within plausible bounds. All perturbations were propagated through both steps of the reconstruction. To quantify the model uncertainty, we computed the point-wise mean absolute deviation of the perturbed model runs from the reference solution. Thus, we estimated the point wise uncertainty $U(x)$ as:

$$U(x) = \frac{1}{N}\sum_{i=1}^{N}|R(x) - E_i(x)|$$

Where $R(x)$ is the "reference" ice-thickness value at pixel x and $E_i(x)$is the ice-thickness value from experiment run $i = 1, \ldots, N$(see section 4.3.2).

4 Results & Discussion

4.1 Ice thickness measurements

The dataset comprises 116.021 individual measurement points, covering a total distance of 232 km across the lower and frontal regions of the surveyed glaciers. This corresponds to 59.0% of the total length of all six survey flights combined. More than half of the measurements were collected over Glaciar Perito Moreno (Fig. 5a), amounting to 60,252 points or 120.5 km of ice-thickness data. The mean ice thickness is 312 m, with a maximum of 706 m recorded in the central part of the glacier trough, approximately 6 km upstream from the terminus. Beneath the central terminus ice flows northward and southward around a peninsula that forms a subglacial ridge, expressed by relatively shallow ice in this region. The ice flowing into the northern channel is 180 to 220 m thick. The eastward facing terminus is shallower with ice thickness values from 130 to 140 m. At a distance of roughly 3 km from the glacier front, ice thickness increases again to about 600 m. Farther upstream, the main tributaries converge into the trunk valley, where a distinctly channelized bedrock topography is evident. Our measurements align well with two previous surveys conducted on the glacier in 1996 and 2010 (Stuefer et al., 2007; Sugiyama et al., 2011). The ice thickness measured by hot-water drilling in 2010 was 515 ± 5 m at a location approximately 4.5 km from the terminus, which agrees well with a close by measurement of 525 ± 26 m obtained during our campaign at −50.49° S, −73.09° W (Sugiyama et al., 2011). At a distance of about 7.5 km from the

https://doi.org/10.5194/essd-2025-678
Preprint. Discussion started: 4 January 2026

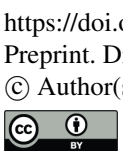

Open Access Earth System Science Data Discussions

terminus, seismic measurements determined an ice thickness of 703 ± 35 m (Stuefer et al., 2007), which is very close (approximately 50 m) to the deepest point of 706 ± 35 m measured during our campaign.

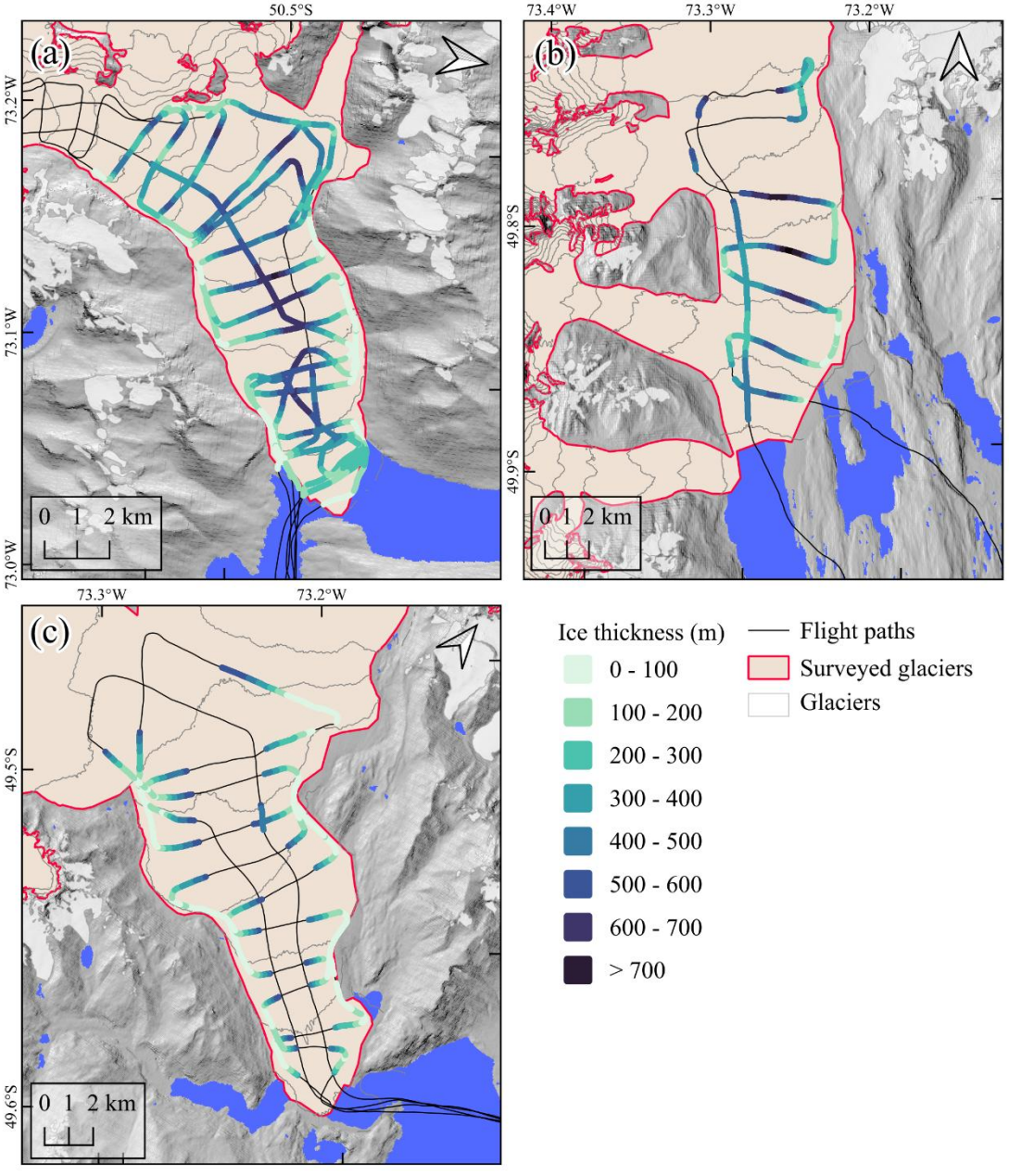

Figure 5 Ice thickness observations for Glaciar Perito Moreno **(a)**, Glaciar Upsala **(b)**, and Glaciar Viedma **(c)**, shown with 100 m surface elevation contours derived from the SRTM DEM. The densest survey grid was collected over Glaciar Perito Moreno **(a)**, revealing a deep glacial trough and a subglacial bedrock ridge at the terminus. Gaps along the flight paths **(a–c)** correspond to areas without identifiable bedrock reflections, which are particularly prevalent in the accumulation area of Glaciar Perito Moreno **(a)** and across the central regions of Glaciar Viedma **(c)**. The greatest ice thickness values, approaching 800 m, are observed along the upper transects of Glaciar Upsala.

https://doi.org/10.5194/essd-2025-678
Preprint. Discussion started: 4 January 2026

We collected 23.479 data points over Glaciar Upsala (Fig. 5b), corresponding to 46.9 km of coverage. The mean ice thickness is 383 m, and the maximum measured thickness is 812 m in the central part of the profile, approximately 9.5 km from the 2024 terminus position. The cross-sections consistently reveal a stepped glacier bed, resulting from the inflow of tributary glacier arms. The deep glacier trough extends throughout all profiles and steepens markedly toward the margins. The ice thickness in the central part of the cross-profile closest to the terminus exceeds 500 m. These values are consistent with previous bathymetric studies conducted in front of the glacier following its large-scale retreat after 2008 (Minowa et al., 2023c).

We collected 32.285 data points over Glaciar Viedma, corresponding to 64.5 km of coverage. The mean thickness is approximately 193 m, and the maximum measured thickness is 623 m. Ice in the central part appears to be thicker, which is plausible given the vast accumulation zone of Glaciar Viedma. The deepest part of the glacial trough appears to narrow progressively toward the terminus. Our assumption that the glacial trough is deeper in the central areas is supported by bathymetric measurements in front of the glacier, where the lake bed near the glacier terminus lies approximately 700 m below lake level (Minowa et al., 2023c).

4.2 Ice thickness reconstruction and bed topography

We used the data compiled in this paper as input for a basin-wide ice thickness reconstruction (Fig. 6). This enables a well-constrained ice thickness field (mean error 10.7 m, n = 116.021, see Appendix Fig. 2) in areas where no direct observations are available. More importantly, due to the well-constrained input dataset, small-scale bedrock features are now represented in these thickness fields. The reconstructions refer to the year 2000 and the corresponding glacier outlines at that time (according to RGI v7.0). In this presentation of the mapping results, we refrain from a comparison to existing maps (REFs). The reason is that we focus on the benefits of the newly collected data, which was not available to previous mapping attempts. As thickness measurements are highly valuable to improve 2D reconstructions (Farinotti et al., 2017, 2021), a comparison of existing map products is of rather limited value. Glaciar Perito Moreno (Fig. 6a), the smallest of the three surveyed glaciers, has a volume of 57.59 km³. The mean ice thickness amounts to 227 m and the largest thickness value is 681 m. Particularly deep regions are found near the

https://doi.org/10.5194/essd-2025-678
Preprint. Discussion started: 4 January 2026

ice divide in the accumulation zone as well as in the central parts of the lower valley, where ice flows through an over deepened glacial trough toward the terminus. The ice thickness field also reveals a subglacial ridge at the terminus that divides the ice flow into two troughs. Glacier Upsala (Fig. 6b), six

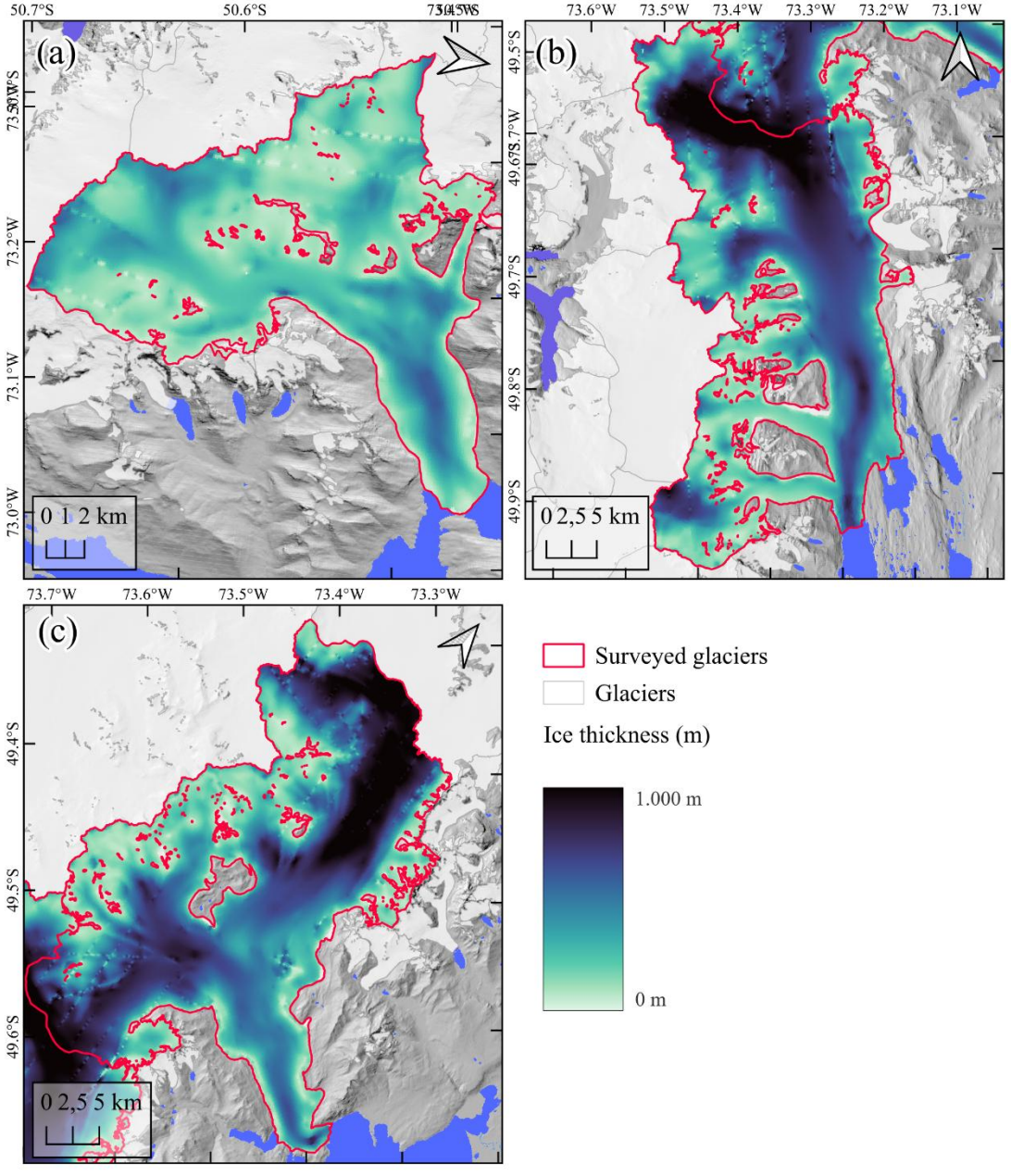

Figure 6 Reconstructed ice thickness fields for Glaciar Perito Moreno **(a)**, Glaciar Upsala **(b)** and Glaciar Viedma **(c).** The reconstructed time step is the year 2000. Outlines in panel **(a – c)** are from the RGI v7.0 and thus also refer to the year 2000.

https://doi.org/10.5194/essd-2025-678
Preprint. Discussion started: 4 January 2026

times larger than Glaciar Perito Moreno, has an ice volume of 340.97 km³. Its mean ice thickness is 449 m, with a maximum of 1.292 m. The greatest thickness occurs in the accumulation zone close to the northern ice divide. From there, ice flows southward through the main valley. The ice thickness distribution toward the tongue is well constrained, and features such as lateral inflow from tributary glaciers are clearly visible in the thickness map. Glaciar Viedma (Fig. 6c) is the largest of the three in both area and volume, with a total basin volume of 432.58 km³. The mean ice thickness is 487 m, and the deepest areas in the northern accumulation zone exceed 1.400 m. Although our profiles do not cover an entire transect, the observations improve the reconstruction by forcing the model to redistribute more ice mass toward the central part of the valley. The resulting ice thickness values are consistent with bathymetric findings near the glacier front (Minowa et al., 2023c).

By knowing the ice thickness distribution, we can also derive maps of the subglacial topography (Fig. 7). We focus here on the frontal areas of the glaciers, where ice is, or will be, in direct contact with water because the bedrock lies below lake level. Maps of the entire basins are provided in the Supplement. For Glaciar Perito Moreno, the frontal area shows a retrograde bed meaning that the bathymetry gets deeper as we move up glacier (Fig. 7a). Below current lake level, a vast subglacial trough is found that extends up to 7.5 km from the current ice front. This trough shows a constriction roughly 5.5 km from the terminus coinciding with the largest ice thickness values measured. After a steep prograde section, the bed elevation rises above lake level. Above the potential lake level a more than 250 m high subglacial ridgeline lies in the central part of the valley. At Glaciar Upsala (Fig. 7b), the bedrock elevation near the terminus lies more than 450 m below lake level. The dashed blue line indicates the lake level and clearly shows where the tributaries have eroded into the main valley. The bedrock remains below lake level up to 14 km upstream from the 2024 terminus position. The bedrock elevation beneath Glaciar Viedma indicates that a large part of the glacier tongue is submerged below the lake level. An approximately 2 km wide and 9 km long section of the lower glacier lies below the level of Lago Argentino. Owing to the vast ice volume,

https://doi.org/10.5194/essd-2025-678
Preprint. Discussion started: 4 January 2026

areas below lake level can still be found in the accumulation zone, almost 30 km upstream from today's

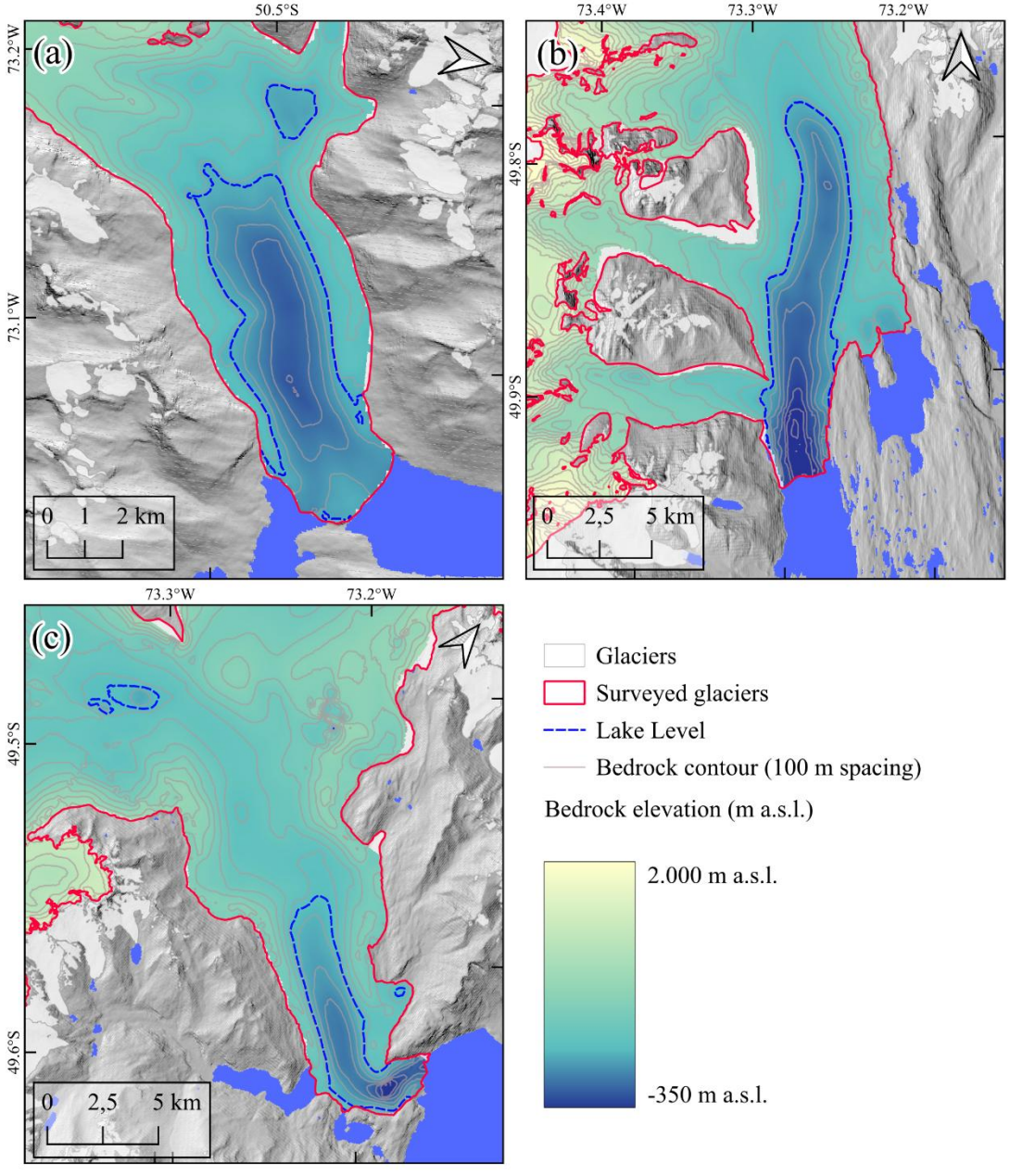

Figure 7 Bedrock elevation of Glaciar Perito Moreno **(a)**, Glaciar Upsala **(b)** and Glaciar Viedma **(c)**. Contour lines **(a-c)** have a 100 m vertical spacing and highlight the deep glacial trough of Glaciar Upsala **(b)** as well as over deepened sections of Glaciar Viedma **(c)** and Glaciar Perito Moreno **(a)**. The blue dashed lines indicate areas at or below lake levels of Lago Viedma **(c)** and Lago Argentino **(a & b)**. Glacier outlines (red lines) are from RGI v7.0 and refer to the year 2000. The lake levels were derived from SRTM. The bedrock elevation of the entire basins can be found in the appendix.

https://doi.org/10.5194/essd-2025-678
Preprint. Discussion started: 4 January 2026

terminus position.

4.3 Uncertainties

4.3.1 Ice thickness measurement uncertainty distribution

Figure 8 presents the resulting uncertainty distribution for the surveyed glaciers. The overall mean ice-thickness uncertainty is 15.6 m (median 14.7 m). Among the three glaciers, Glaciar Viedma shows the lowest average uncertainty (11.0 m, median 7.6 m), Glaciar Upsala the highest (19.8 m, median 19.0 m), and Glaciar Perito Moreno lies in between (16.4 m, median 15.5 m).

To assess the consistency of the dataset, we compared the ice-thickness values at cross points. The entire dataset shows a median misfit of 9 m with a standard deviation of σ = 13.92 m (n = 49). For individual glaciers, Glaciar Perito Moreno has a median misfit of 10 m (σ = 14.17 m, n = 36), Glaciar Upsala a median misfit of 10 m (σ = 14.17 m, n = 4), and Glaciar Viedma a median misfit of 4 m (σ = 13.92 m, n = 9).

Gaps in the uncertainty map mark areas where no distinct bedrock reflections were visible in the radargrams. We attribute this to several characteristics of the surveyed glaciers. First, all three glaciers are temperate and therefore contain large amounts of liquid water, which attenuates the radar signal and limits the maximum detectable depth. Although our system is optimized for operation over temperate ice, some regions are likely too deep to return a measurable signal. Furthermore, the strongly crevassed and often water-filled surfaces of these glaciers scatter and or attenuate the radar energy. In particular, oblique scattering from crevasses can obscure echoes from the underlying bedrock (Peters et al., 2005). In addition, the glaciers flow around nunataks in their accumulation zones, transporting debris onto and within the ice, which causes further signal scattering or attenuation depending on the debris layer thickness. This effect is evident at the beginning (left side) of the radargram in Fig. 3a and in the central section of Fig. 4a. Although Glaciar Perito Moreno was surveyed at the end of the ablation season, the surface above ~950 m a.s.l. was still covered by (likely wet) snow, which we assume prevented bedrock

https://doi.org/10.5194/essd-2025-678
Preprint. Discussion started: 4 January 2026

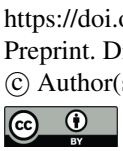

reflections in this region. Strong katabatic winds also affected this area, forcing us to fly at higher altitudes above the surface, thereby increasing signal decay before the radar wave reached the ice.

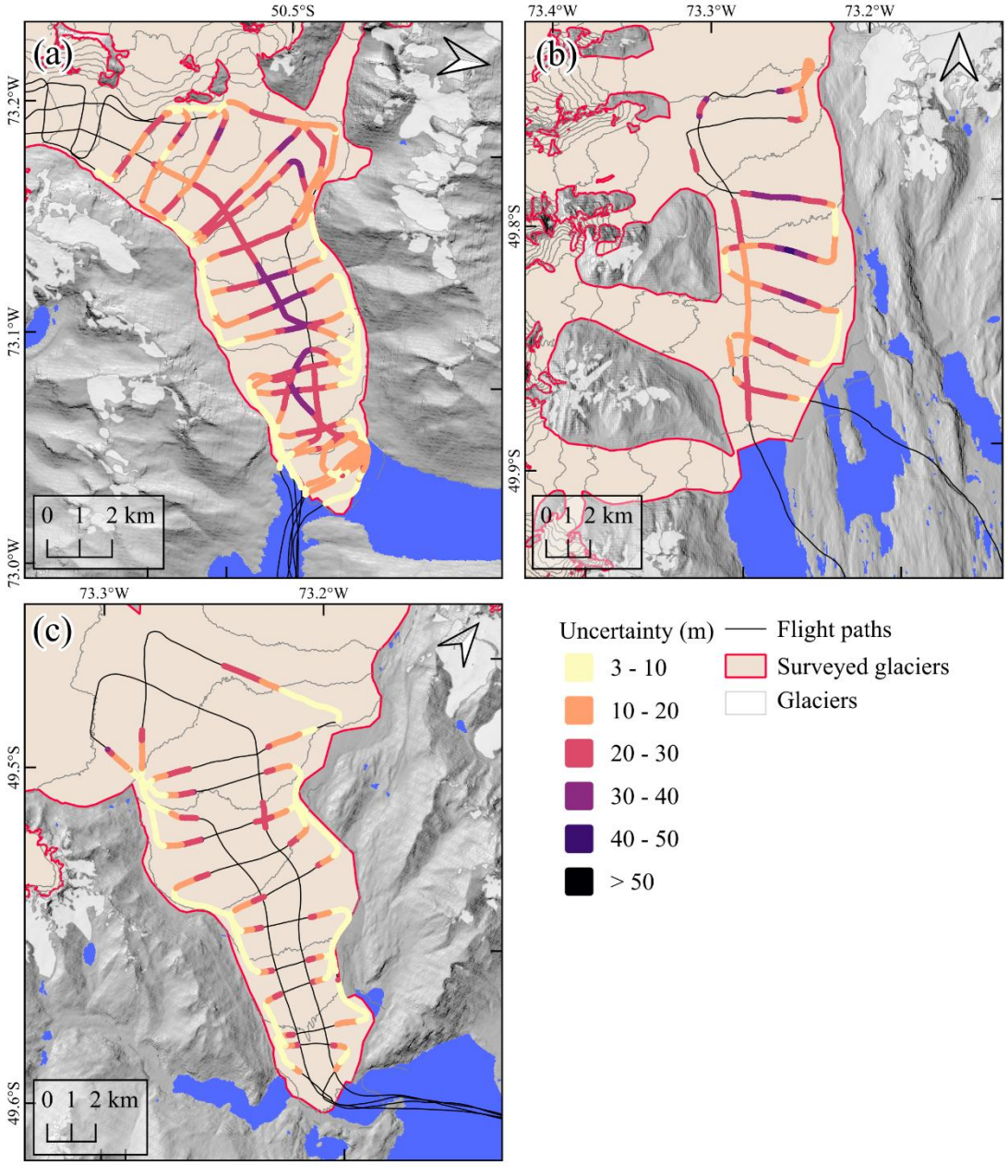

Figure 8 Estimated uncertainties in ice thickness derived from radar data acquisition, quantified following the methodology of Lapazaran et al. (2016), for Glaciar Perito Moreno **(a)**, Glaciar Upsala **(b)**, and Glaciar Viedma **(c)**. Variations in uncertainty are primarily controlled by the local bedrock gradient and radar travel time (i.e., local ice thickness). Consequently, the largest uncertainties occur in areas of greatest ice thickness. Background is a hill shaded DEM, glacier outlines and lake extents as in Fig. 1.

https://doi.org/10.5194/essd-2025-678
Preprint. Discussion started: 4 January 2026

4.3.2 Ice thickness reconstruction uncertainty fields

Figure 9 displays the uncertainty maps for the surveyed glaciers. The highest uncertainties occur in areas with (i) no nearby observations, (ii) large ice thickness, (iii) poorly constrained velocity data, or a combination of these factors. For example, in the central part of the lower regions of Glaciar Viedma (Fig. 9c), where our GPR profiles do not span the full glacier width, uncertainties in the cross-sectional centre are relatively large. Uncertainties here range from 100 to 150 m, which is plausible, given the depth measured by bathymetry measurements close to the today's glaciers terminus (Minowa et al., 2023d). Conversely, in the ablation zone of Glaciar Perito Moreno (Fig. 9a), which was surveyed densely, the mean uncertainty remains comparatively small. The patchy uncertainty patterns near the termini of Glaciar Upsala and Glaciar Viedma (Fig. 9b–c) originate from the experiments with perturbed viscosity scaling. In these areas, high-resolution bathymetry introduced steep spatial viscosity gradients that could not be smoothed in the second reconstruction step because no velocity data were available. The integrated uncertainty corresponds to 155 km^3, or 18.6% of the reference volume (total of 831 km^3).

https://doi.org/10.5194/essd-2025-678
Preprint. Discussion started: 4 January 2026

400

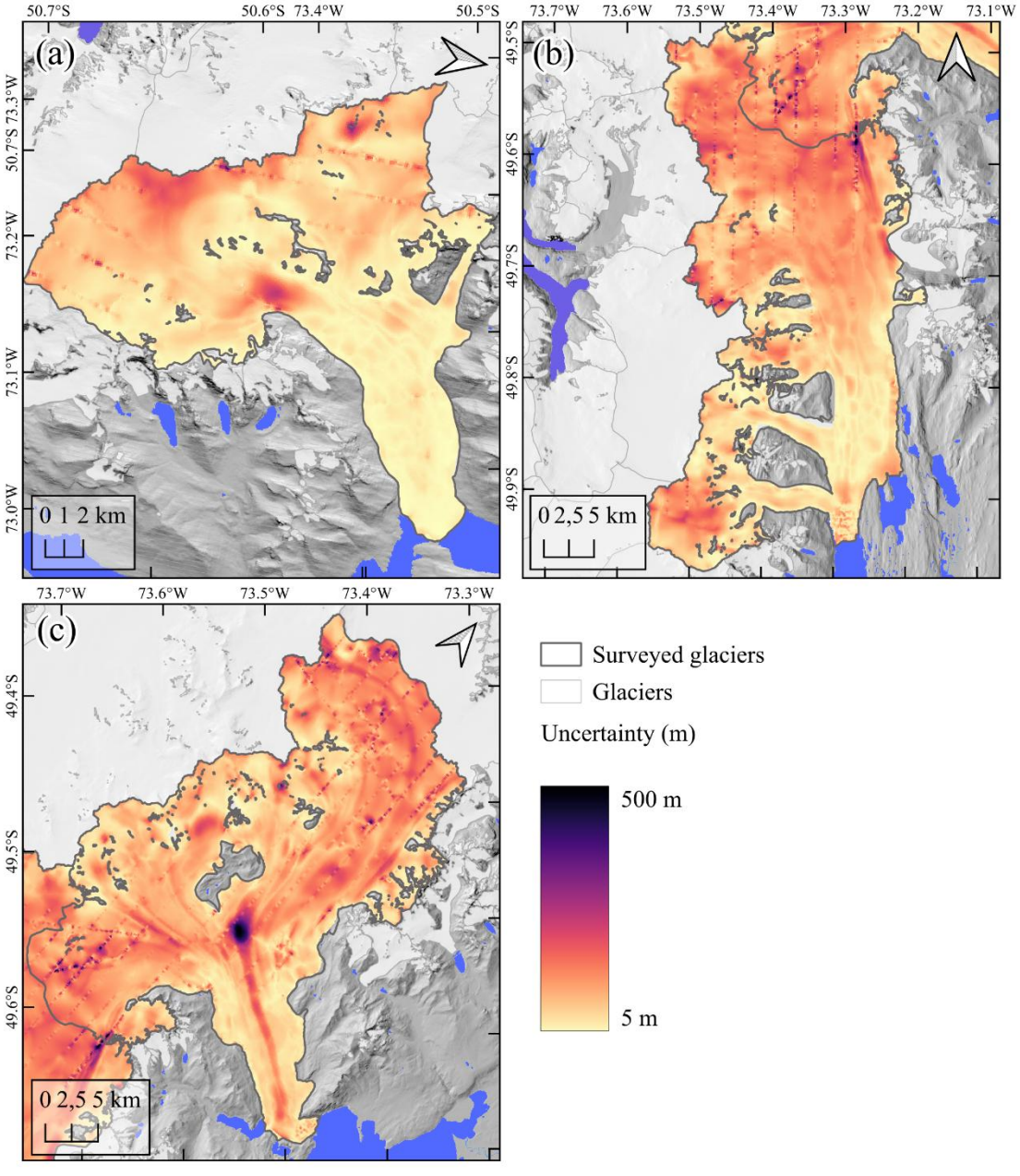

Figure 9 Absolute mean uncertainty in m from all model runs, for Glaciar Perito Moreno **(a)**, Glaciar Upsala **(b)**, and Glaciar Viedma **(c)**. Variations in uncertainty are primarily controlled by depth and distance to measurements. Consequently, the largest uncertainties occur in areas which have either no measurements in proximity or where the thickest ice was observed.

https://doi.org/10.5194/essd-2025-678
Preprint. Discussion started: 4 January 2026

5 Data availability

The complete dataset, including the unprocessed (single files) and processed radar data (combined .csv file), point thickness measurements, bed elevations with corresponding uncertainties, ice thickness maps, corresponding ice thickness uncertainty maps and subglacial topography maps, is publicly available on Zenodo at: [DOI: https://doi.org/10.5281/zenodo.17802904, (Koch et al., 2025a)].

6 Conclusions

In this paper, we present densely gridded ground-penetrating radar measurements from the lower regions of Glaciar Perito Moreno, Upsala, and Viedma. In total, we collected 116.021 individual measurement points along 232 km of transects, covering an area of 243 km² over ice collected during two campaigns in 2022 and 2024. Ice thicknesses of up to 800 m were measured, allowing us to constrain the bedrock topography beneath all three glaciers. Our observations were further incorporated into a well-established ice thickness reconstruction method to derive basin-wide ice thickness distributions and the corresponding subglacial topography. These datasets shed first light on the glacier geometry for three of the largest outlet glaciers in Argentina and the Southern Patagonian Icefield. We expect this dataset to be of significant value for future studies on glacier retreat and to contribute to a better understanding of the climatic drivers influencing glacier dynamics within the largest temperate ice field in the Southern Hemisphere, an area characterized by heterogeneous glacier retreat.

Author contributions

M.K., J.F.F. and M.B. conceptualized the study, M.K., P.S., N.B., J.F.F. and M.B. carried out the field work, M.K. and N.B. processed and interpreted the ice thickness measurements, J.B. and J.F.F. incorporated the new observations in the ice thickness reconstruction, J.B. and M.K. performed the uncertainty analysis of the ice thickness reconstruction, D.F. processed the GNSS data, M.K. wrote the manuscript and compiled all figures, all co-authors contributed to the final version of the submitted manuscript.

https://doi.org/10.5194/essd-2025-678
Preprint. Discussion started: 4 January 2026

Competing interests

The authors declare no conflict of interest.

Acknowledgements

The authors would like to gratefully acknowledge the scientific support and HPC resources provided by the Erlangen National High Performance Computing Centre (NHR@FAU) of the Friedrich-Alexander-Universität Erlangen-Nürnberg (FAU). NHR funding is provided by federal and Bavarian state authorities, and NHR@FAU hardware is partially funded by the German Research Foundation (DFG, project number 440719683). J.B. thanks the support of ANID/DAAD through the doctoral scholarships program. Special thanks go to Steffen Welsch for his invaluable support during both of our field campaigns.

Financial support

M.K. was funded by the ITERATE project (BR2105/28-1, FU1032/12-1) financed by the German Research Foundation (DFG). J.J.F. received funding from the European Union's Horizon 2020 research and innovation programme via the European Research Council (ERC) as a Starting Grant (FRAGILE project) under grant agreement No 948290.

https://doi.org/10.5194/essd-2025-678
Preprint. Discussion started: 4 January 2026

References

Abdel Jaber, W., Rott, H., Floricioiu, D., Wuite, J., and Miranda, N.: Heterogeneous spatial and temporal pattern of surface elevation change and mass balance of the Patagonian ice fields between 2000 and 2016, The Cryosphere, 13, 2511–2535, https://doi.org/10.5194/tc-13-2511-2019, 2019.

Aguayo, R., Maussion, F., Schuster, L., Schaefer, M., Caro, A., Schmitt, P., Mackay, J., Ultee, L., Leon-Muñoz, J., and Aguayo, M.: Unravelling the sources of uncertainty in glacier runoff projections in the Patagonian Andes (40–56° S), The Cryosphere, 18, 5383–5406, https://doi.org/10.5194/tc-18-5383-2024, 2024.

Aniya, M., Sato, H., Naruse, R., Skvarca, P., and Casassa, G.: Recent Glacier Variations in the Southern Patagonia Icefield, South America, Arctic and Alpine Research, 29, 1, https://doi.org/10.2307/1551831, 1997.

Bamber, J. L., Westaway, R. M., Marzeion, B., and Wouters, B.: The land ice contribution to sea level during the satellite era, Environ. Res. Lett., 13, 063008, https://doi.org/10.1088/1748-9326/aac2f0, 2018.

Beck, H. E., Zimmermann, N. E., McVicar, T. R., Vergopolan, N., Berg, A., and Wood, E. F.: Present and future Köppen-Geiger climate classification maps at 1-km resolution, Sci Data, 5, 180214, https://doi.org/10.1038/sdata.2018.214, 2018.

Benn, D. I., Warren, C. R., and Mottram, R. H.: Calving processes and the dynamics of calving glaciers, Earth-Science Reviews, 82, 143–179, https://doi.org/10.1016/j.earscirev.2007.02.002, 2007.

Blindow, N., Suckro, S. K., Rückamp, M., Braun, M., Schindler, M., Breuer, B., Saurer, H., Simões, J. C., and Lange, M. A.: Geometry and thermal regime of the King George Island ice cap, Antarctica, from GPR and GPS, Ann. Glaciol., 51, 103–109, https://doi.org/10.3189/172756410791392691, 2010.

Blindow, N., Salat, C., Gundelach, V., Buschmann, U., and Kahnt, W.: Performance and calibration of the helicoper GPR system BGR-P30, in: 2011 6th International Workshop on Advanced Ground Penetrating Radar (IWAGPR), 2011 6th International Workshop on Advanced Ground Penetrating Radar (IWAGPR 2011), Aachen, Germany, 1–5, https://doi.org/10.1109/IWAGPR.2011.5963896, 2011.

Blindow, N., Salat, C., and Casassa, G.: Airborne GPR sounding of deep temperate glaciers — Examples from the Northern Patagonian Icefield, in: 2012 14th International Conference on Ground Penetrating Radar (GPR), 2012 14th International Conference on Ground Penetrating Radar (GPR), Shanghai, 664–669, https://doi.org/10.1109/ICGPR.2012.6254945, 2012.

Bojinski, S., Verstraete, M., Peterson, T. C., Richter, C., Simmons, A., and Zemp, M.: The Concept of Essential Climate Variables in Support of Climate Research, Applications, and Policy, Bulletin of the American Meteorological Society, 95, 1431–1443, https://doi.org/10.1175/BAMS-D-13-00047.1, 2014.

Bosson, J. B., Huss, M., Cauvy-Fraunié, S., Clément, J. C., Costes, G., Fischer, M., Poulenard, J., and Arthaud, F.: Future emergence of new ecosystems caused by glacial retreat, Nature, 620, 562–569, https://doi.org/10.1038/s41586-023-06302-2, 2023.

https://doi.org/10.5194/essd-2025-678
Preprint. Discussion started: 4 January 2026

Braun, M. H., Malz, P., Sommer, C., Farías-Barahona, D., Sauter, T., Casassa, G., Soruco, A., Skvarca, P., and Seehaus, T. C.: Constraining glacier elevation and mass changes in South America, Nature Clim Change, 9, 130–136, https://doi.org/10.1038/s41558-018-0375-7, 2019.

Casassa, G., Rodríguez, J. L., and Loriaux, T.: A New Glacier Inventory for the Southern Patagonia Icefield and Areal Changes 1986–2000, in: Global Land Ice Measurements from Space, edited by: Kargel, J. S., Leonard, G. J., Bishop, M. P., Kääb, A., and Raup, B. H., Springer Berlin Heidelberg, Berlin, Heidelberg, 639–660, https://doi.org/10.1007/978-3-540-79818-7_27, 2014.

Dorigo, W., Dietrich, S., Aires, F., Brocca, L., Carter, S., Cretaux, J.-F., Dunkerley, D., Enomoto, H., Forsberg, R., Güntner, A., Hegglin, M. I., Hollmann, R., Hurst, D. F., Johannessen, J. A., Kummerow, C., Lee, T., Luojus, K., Looser, U., Miralles, D. G., Pellet, V., Recknagel, T., Vargas, C. R., Schneider, U., Schoeneich, P., Schröder, M., Tapper, N., Vuglinsky, V., Wagner, W., Yu, L., Zappa, L., Zemp, M., and Aich, V.: Closing the Water Cycle from Observations across Scales: Where Do We Stand?, Bulletin of the American Meteorological Society, 102, E1897–E1935, https://doi.org/10.1175/BAMS-D-19-0316.1, 2021.

European Space Agency and Airbus: Copernicus DEM, https://doi.org/10.5270/ESA-c5d3d65, 2022.

Farinotti, D., Brinkerhoff, D. J., Clarke, G. K. C., Fürst, J. J., Frey, H., Gantayat, P., Gillet-Chaulet, F., Girard, C., Huss, M., Leclercq, P. W., Linsbauer, A., Machguth, H., Martin, C., Maussion, F., Morlighem, M., Mosbeux, C., Pandit, A., Portmann, A., Rabatel, A., Ramsankaran, R., Reerink, T. J., Sanchez, O., Stentoft, P. A., Singh Kumari, S., Van Pelt, W. J. J., Anderson, B., Benham, T., Binder, D., Dowdeswell, J. A., Fischer, A., Helfricht, K., Kutuzov, S., Lavrentiev, I., McNabb, R., Gudmundsson, G. H., Li, H., and Andreassen, L. M.: How accurate are estimates of glacier ice thickness? Results from ITMIX, the Ice Thickness Models Intercomparison eXperiment, The Cryosphere, 11, 949–970, https://doi.org/10.5194/tc-11-949-2017, 2017.

Farinotti, D., Brinkerhoff, D. J., Fürst, J. J., Gantayat, P., Gillet-Chaulet, F., Huss, M., Leclercq, P. W., Maurer, H., Morlighem, M., Pandit, A., Rabatel, A., Ramsankaran, R., Reerink, T. J., Robo, E., Rouges, E., Tamre, E., Van Pelt, W. J. J., Werder, M. A., Azam, M. F., Li, H., and Andreassen, L. M.: Results from the Ice Thickness Models Intercomparison eXperiment Phase 2 (ITMIX2), Front. Earth Sci., 8, 571923, https://doi.org/10.3389/feart.2020.571923, 2021.

Frank, T., Åkesson, H., De Fleurian, B., Morlighem, M., and Nisancioglu, K. H.: Geometric controls of tidewater glacier dynamics, The Cryosphere, 16, 581–601, https://doi.org/10.5194/tc-16-581-2022, 2022.

Fürst, J. J., Gillet-Chaulet, F., Benham, T. J., Dowdeswell, J. A., Grabiec, M., Navarro, F., Pettersson, R., Moholdt, G., Nuth, C., Sass, B., Aas, K., Fettweis, X., Lang, C., Seehaus, T., and Braun, M.: Application of a two-step approach for mapping ice thickness to various glacier types on Svalbard, The Cryosphere, 11, 2003–2032, https://doi.org/10.5194/tc-11-2003-2017, 2017.

Fürst, J. J., Navarro, F., Gillet-Chaulet, F., Huss, M., Moholdt, G., Fettweis, X., Lang, C., Seehaus, T., Ai, S., Benham, T. J., Benn, D. I., Björnsson, H., Dowdeswell, J. A., Grabiec, M., Kohler, J., Lavrentiev, I., Lindbäck, K., Melvold, K., Pettersson,

R., Rippin, D., Saintenoy, A., Sánchez-Gámez, P., Schuler, T. V., Sevestre, H., Vasilenko, E., and Braun, M. H.: The Ice-Free Topography of Svalbard, Geophysical Research Letters, 45, https://doi.org/10.1029/2018GL079734, 2018.

Fürst, J. J., Farías-Barahona, D., Blindow, N., Casassa, G., Gacitúa, G., Koppes, M., Lodolo, E., Millan, R., Minowa, M., Mouginot, J., Pętlicki, M., Rignot, E., Rivera, A., Skvarca, P., Stuefer, M., Sugiyama, S., Uribe, J., Zamora, R., Braun, M. H., Gillet-Chaulet, F., Malz, P., Meier, W. J.-H., and Schaefer, M.: The foundations of the Patagonian icefields, Commun Earth Environ, 5, 142, https://doi.org/10.1038/s43247-023-01193-7, 2024a.

Fürst, J. J., Farías-Barahona, D., Blindow, N., Casassa, G., Gacitúa, G., Koppes, M., Lodolo, E., Millan, R., Minowa, M., Mouginot, J., Pętlicki, M., Rignot, E., Rivera, A., Skvarca, P., Stuefer, M., Sugiyama, S., Uribe, J., Zamora, R., Braun, M. H., Gillet-Chaulet, F., Malz, P., Meier, W. J.-H., and Schaefer, M.: The foundations of the Patagonian icefields, Commun Earth Environ, 5, 142, https://doi.org/10.1038/s43247-023-01193-7, 2024b.

Gao, X., Podd, F. J. W., Van Verre, W., Daniels, D. J., and Peyton, A. J.: Investigating the Performance of Bi-Static GPR Antennas for Near-Surface Object Detection, Sensors, 19, 170, https://doi.org/10.3390/s19010170, 2019.

Garreaud, R., Lopez, P., Minvielle, M., and Rojas, M.: Large-Scale Control on the Patagonian Climate, Journal of Climate, 26, 215–230, https://doi.org/10.1175/JCLI-D-12-00001.1, 2013.

Glasser, N. F., Harrison, S., Jansson, K. N., Anderson, K., and Cowley, A.: Global sea-level contribution from the Patagonian Icefields since the Little Ice Age maximum, Nature Geosci, 4, 303–307, https://doi.org/10.1038/ngeo1122, 2011.

Gourlet, P., Rignot, E., Rivera, A., and Casassa, G.: Ice thickness of the northern half of the Patagonia Icefields of South America from high-resolution airborne gravity surveys, Geophysical Research Letters, 43, 241–249, https://doi.org/10.1002/2015GL066728, 2016.

Hugonnet, R., McNabb, R., Berthier, E., Menounos, B., Nuth, C., Girod, L., Farinotti, D., Huss, M., Dussaillant, I., Brun, F., and Kääb, A.: Accelerated global glacier mass loss in the early twenty-first century, Nature, 592, 726–731, https://doi.org/10.1038/s41586-021-03436-z, 2021.

Koch, M., Berkhoff, J., Blindow, N., Farías-Barahona, D., Skvarca, P., Fürst, J. J., and Braun, M.: Ground Penetrating Radar Data, Ice thickness fields and bedrock topography maps of Glaciar Perito Moreno, Viedma and Upsala (2), https://doi.org/10.5281/zenodo.17802904, 2025a.

Koch, M., Sommer, C., Blindow, N., Lutz, K., Skvarca, P., Ruiz, L., Rizzoli, P., Bueso-Bello, J.-L., Fürst, J. J., and Braun, M. H.: The state and fate of Glaciar Perito Moreno Patagonia, Commun Earth Environ, 6, 572, https://doi.org/10.1038/s43247-025-02515-7, 2025b.

Lapazaran, J. J., Otero, J., Martín-Español, A., and Navarro, F. J.: On the errors involved in ice-thickness estimates I: ground-penetrating radar measurement errors, J. Glaciol., 62, 1008–1020, https://doi.org/10.1017/jog.2016.93, 2016.

Lenaerts, J. T. M., Van Den Broeke, M. R., Van Wessem, J. M., Van De Berg, W. J., Van Meijgaard, E., Van Ulft, L. H., and Schaefer, M.: Extreme Precipitation and Climate Gradients in Patagonia Revealed by High-Resolution Regional Atmospheric Climate Modeling, Journal of Climate, 27, 4607–4621, https://doi.org/10.1175/JCLI-D-13-00579.1, 2014.

Lippl, S., Blindow, N., Fürst, J. J., Marinsek, S., Seehaus, T. C., and Braun, M. H.: Uncertainty Assessment of Ice Discharge Using GPR-Derived Ice Thickness from Gourdon Glacier, Antarctic Peninsula, Geosciences, 10, 12, https://doi.org/10.3390/geosciences10010012, 2019.

McDonnell, M., Rupper, S., and Forster, R.: Quantifying Geodetic Mass Balance of the Northern and Southern Patagonian Icefields Since 1976, Front. Earth Sci., 10, 813574, https://doi.org/10.3389/feart.2022.813574, 2022.

Millan, R., Rignot, E., Rivera, A., Martineau, V., Mouginot, J., Zamora, R., Uribe, J., Lenzano, G., De Fleurian, B., Li, X., Gim, Y., and Kirchner, D.: Ice Thickness and Bed Elevation of the Northern and Southern Patagonian Icefields, Geophysical Research Letters, 46, 6626–6635, https://doi.org/10.1029/2019GL082485, 2019.

Minowa, M., Schaefer, M., Sugiyama, S., Sakakibara, D., and Skvarca, P.: Frontal ablation and mass loss of the Patagonian icefields, Earth and Planetary Science Letters, 561, 116811, https://doi.org/10.1016/j.epsl.2021.116811, 2021a.

Minowa, M., Schaefer, M., Sugiyama, S., Sakakibara, D., and Skvarca, P.: Frontal ablation and mass loss of the Patagonian icefields, Earth and Planetary Science Letters, 561, 116811, https://doi.org/10.1016/j.epsl.2021.116811, 2021b.

Minowa, M., Skvarca, P., and Fujita, K.: Climate and Surface Mass Balance at Glaciar Perito Moreno, Southern Patagonia, Journal of Climate, 36, 625–641, https://doi.org/10.1175/JCLI-D-22-0294.1, 2023a.

Minowa, M., Schaefer, M., and Skvarca, P.: Effects of topography on dynamics and mass loss of lake-terminating glaciers in southern Patagonia, J. Glaciol., 1–18, https://doi.org/10.1017/jog.2023.42, 2023b.

Minowa, M., Schaefer, M., and Skvarca, P.: Effects of topography on dynamics and mass loss of lake-terminating glaciers in southern Patagonia, J. Glaciol., 69, 1580–1597, https://doi.org/10.1017/jog.2023.42, 2023c.

Minowa, M., Schaefer, M., and Skvarca, P.: Water depth observed in front of lake-terminating glaciers in Patagonia (v1), https://doi.org/10.5281/ZENODO.7112456, 2023d.

Naruse, R., Skvarca, P., and Takeuchi, Y.: Thinning and retreat of Glaciar Upsala, and an estimate of annual ablation changes in southern Patagonia, Ann. Glaciol., 24, 38–42, https://doi.org/10.3189/S0260305500011903, 1997.

Peters, M. E., Blankenship, D. D., and Morse, D. L.: Analysis techniques for coherent airborne radar sounding: Application to West Antarctic ice streams, J. Geophys. Res., 110, 2004JB003222, https://doi.org/10.1029/2004JB003222, 2005.

RGI Consortium: Randolph Glacier Inventory - A Dataset of Global Glacier Outlines, Version 7, https://doi.org/10.5067/F6JMOVY5NAVZ, 2023.

Rounce, D. R., Hock, R., Maussion, F., Hugonnet, R., Kochtitzky, W., Huss, M., Berthier, E., Brinkerhoff, D., Compagno, L., Copland, L., Farinotti, D., Menounos, B., and McNabb, R. W.: Global glacier change in the 21st century: Every increase in temperature matters, Science, 379, 78–83, https://doi.org/10.1126/science.abo1324, 2023.

Rutishauser, A., Maurer, H., and Bauder, A.: Helicopter-borne ground-penetrating radar investigations on temperate alpine glaciers: A comparison of different systems and their abilities for bedrock mapping, GEOPHYSICS, 81, WA119–WA129, https://doi.org/10.1190/geo2015-0144.1, 2016.

Sakakibara, D., Sugiyama, S., Sawagaki, T., Marinsek, S., and Skvarca, P.: Rapid retreat, acceleration and thinning of Glaciar Upsala, Southern Patagonia Icefield, initiated in 2008, Ann. Glaciol., 54, 131–138, https://doi.org/10.3189/2013AoG63A236, 2013.

Sauter, T.: Revisiting extreme precipitation amounts over southern South America and implications for the Patagonian Icefields, Hydrol. Earth Syst. Sci., 24, 2003–2016, https://doi.org/10.5194/hess-24-2003-2020, 2020.

Schaefer, M., Machguth, H., Falvey, M., Casassa, G., and Rignot, E.: Quantifying mass balance processes on the Southern Patagonia Icefield, The Cryosphere, 9, 25–35, https://doi.org/10.5194/tc-9-25-2015, 2015.

Skvarca, P. and Naruse, R.: Overview of the ice-dam formation and collapse of Glaciar Perito Moreno, southern Patagonia, in 2003/04, J. Glaciol., 52, 318–320, https://doi.org/10.3189/S0022143000208666, 2006.

Sommer, C., Fürst, J. J., Huss, M., and Braun, M. H.: Constraining regional glacier reconstructions using past ice thickness of deglaciating areas – a case study in the European Alps, The Cryosphere, 17, 2285–2303, https://doi.org/10.5194/tc-17-2285-2023, 2023.

Stuefer, M., Rott, H., and Skvarca, P.: Glaciar Perito Moreno, Patagonia: climate sensitivities and glacier characteristics preceding the 2003/04 and 2005/06 damming events, J. Glaciol., 53, 3–16, https://doi.org/10.3189/172756507781833848, 2007.

Sugiyama, S., Skvarca, P., Naito, N., Enomoto, H., Tsutaki, S., Tone, K., Marinsek, S., and Aniya, M.: Ice speed of a calving glacier modulated by small fluctuations in basal water pressure, Nature Geosci, 4, 597–600, https://doi.org/10.1038/ngeo1218, 2011.

The GlaMBIE Team, Zemp, M., Jakob, L., Dussaillant, I., Nussbaumer, S. U., Gourmelen, N., Dubber, S., A, G., Abdullahi, S., Andreassen, L. M., Berthier, E., Bhattacharya, A., Blazquez, A., Boehm Vock, L. F., Bolch, T., Box, J., Braun, M. H., Brun, F., Cicero, E., Colgan, W., Eckert, N., Farinotti, D., Florentine, C., Floricioiu, D., Gardner, A., Harig, C., Hassan, J., Hugonnet, R., Huss, M., Jóhannesson, T., Liang, C.-C. A., Ke, C.-Q., Khan, S. A., King, O., Kneib, M., Krieger, L., Maussion, F., Mattea, E., McNabb, R., Menounos, B., Miles, E., Moholdt, G., Nilsson, J., Pálsson, F., Pfeffer, J., Piermattei, L., Plummer, S., Richter, A., Sasgen, I., Schuster, L., Seehaus, T., Shen, X., Sommer, C., Sutterley, T., Treichler, D., Velicogna, I., Wouters, B., Zekollari, H., and Zheng, W.: Community estimate of global glacier mass changes from 2000 to 2023, Nature, 639, 382–388, https://doi.org/10.1038/s41586-024-08545-z, 2025.

Viale, M. and Garreaud, R.: Orographic effects of the subtropical and extratropical Andes on upwind precipitating clouds, JGR Atmospheres, 120, 4962–4974, https://doi.org/10.1002/2014JD023014, 2015.

World Glacier Monitoring Service (WGMS): Glacier Thickness Database (GlaThiDa), https://doi.org/10.5904/WGMS-GLATHIDA-2020-10, 2020.

Zekollari, H., Huss, M., Schuster, L., Maussion, F., Rounce, D. R., Aguayo, R., Champollion, N., Compagno, L., Hugonnet, R., Marzeion, B., Mojtabavi, S., and Farinotti, D.: Twenty-first century global glacier evolution under CMIP6 scenarios and the role of glacier-specific observations, The Cryosphere, 18, 5045–5066, https://doi.org/10.5194/tc-18-5045-2024, 2024.